

PAPER

Assessing the merits of resonant magnetic perturbations with different toroidal mode numbers for controlling edge localised modes

To cite this article: I.T. Chapman *et al* 2014 *Nucl. Fusion* **54** 123003

View the [article online](#) for updates and enhancements.

Related content

- [Overview of MAST results](#)
I.T. Chapman, J. Adamek, R.J. Akers *et al.*
- [Understanding edge-localized mode mitigation by resonant magnetic perturbations on MAST](#)
A. Kirk, I.T. Chapman, Yueqiang Liu *et al.*
- [Effect of resonant magnetic perturbations with toroidal mode numbers of 4 and 6 on edge-localized modes in single null H-mode plasmas in MAST](#)
A Kirk, I T Chapman, J Harrison *et al.*

Recent citations

- [Edge plasma properties with 3D magnetic perturbations in RFX-mod](#)
M. Agostini *et al*
- [Advances in understanding and utilising ELM control in JET](#)
I T Chapman *et al*
- [Non-axisymmetric ideal equilibrium and stability of ITER plasmas with rotating RMPs](#)
C.J. Ham *et al*

Assessing the merits of resonant magnetic perturbations with different toroidal mode numbers for controlling edge localised modes

I.T. Chapman¹, A. Kirk¹, R.J. Akers¹, C.J. Ham¹, J.R. Harrison¹,
J. Hawke², Y.Q. Liu¹, K.G. McClements¹, S. Pamela¹,
S. Saarelma¹, R. Scannell¹, A.J. Thornton¹ and The MAST Team

¹ CCFE, Culham Science Centre, Abingdon, Oxon, OX14 3DB, UK

² FOM Institute DIFFER Dutch Institute for Fundamental Energy Research, 3430 BE Nieuwegein, Netherlands

Received 21 March 2014, revised 1 August 2014

Accepted for publication 5 August 2014

Published 16 October 2014

Abstract

An increase in ELM frequency has been demonstrated in MAST by applying resonant magnetic perturbations (RMPs) with toroidal mode number, $n_{\text{RMP}} = 2, 3, 4, 6$. It has been observed that the mitigated ELM frequency increases with the amplitude of the applied field provided it is above a critical threshold. This threshold value depends on the mode number of the RMP, with higher n_{RMP} having a larger critical value. For the same ELM frequency, the reduction in the peak heat load on the divertor plates is approximately the same for all RMP configurations. The RMPs give rise to perturbations to the plasma shape, with lobe structures occurring due to the tangled magnetic fields near the X-point, and corrugations of the plasma boundary at the midplane. The X-point lobe length increases linearly with the applied field when above a threshold, with RMPs of higher toroidal mode number giving rise to longer lobes for the same applied resonant field. Similarly, the midplane displacements increase with the applied field strength, though the corrugation amplitude is less dependent upon the RMP configuration. For all n_{RMP} , the RMPs result in enhanced particle transport and a reduction in the pedestal pressure gradient caused by an increased pedestal width, which is found to be consistent with a decrease in the critical pressure at which infinite- n ballooning modes are driven unstable in non-axisymmetric plasmas. The plasma rotation braking is strongest for lowest n_{RMP} whilst the degradation of access to H-mode resultant from the application of RMPs are non-monotonic in n_{RMP} , with the optimal case for both occurring for $n_{\text{RMP}} = 4$. Whilst there are advantages and disadvantages for all RMP configurations, the configurations found to be optimised in terms of pedestal degradation, access to H-mode, plasma rotation and distortion to the plasma configuration in MAST are $n_{\text{RMP}} = 3$ or 4, consistent with the configurations anticipated for use in ITER.

Keywords: ELM mitigation, MAST, RMPs

(Some figures may appear in colour only in the online journal)

1. Introduction and background

Edge localised modes (ELMs) occur at the periphery of tokamak plasmas which operate in a high-confinement regime [1]. In this regime of improved confinement, a transport barrier, or ‘pedestal’, forms at the edge, leading to a strong pressure gradient. The high gradient in the pressure and current density which occur in the pedestal region drive peeling–ballooning instabilities [2, 3], which are believed to be manifest as ELMs [1]. However, empirical scaling of the energy released by ELMs suggests that the heat loads on the plasma facing components in ITER will be intolerable unless mitigated. In order to ensure an appropriate lifetime of plasma

facing components in ITER, robust ELM control is required, either suppressing the ELMs completely or, at least, reducing the heat flux per ELM which is incident on the divertor plates [4]. One such control scheme is the application of resonant magnetic perturbations (RMPs), which perturb the magnetic field in the pedestal region, locally degrading the confinement.

RMPs have been applied to completely suppress ELMs in DIII-D [5, 6] and KSTAR [7], or to mitigate ELMs—that is to say increase their frequency and reduce their amplitude—in ASDEX Upgrade [8, 9], MAST [10–12] and JET [13, 14]. It is expected that ITER will use RMPs to control ELMs, with the non-axisymmetric fields having a toroidal periodicity of $n = 3$ or $n = 4$ (see review article [15] and references therein). This

choice of mode number was based on DIII-D results which showed that $n = 3$ fields could suppress ELMs [5, 19] and calculations which suggested that in-vessel coils could provide sufficient perturbation to the plasma edge magnetic topology to have the same effect in ITER [16–18]. The in-vessel control coils for ITER were specified upon the basis of vacuum modelling [17, 18] which stipulated the necessary fields such that the RMP-induced islands overlapped across a certain width of the minor radius which was found to be correlated with ELM suppression in DIII-D experiments [19]. The present ITER design [20] has a set of 27 in-vessel six-turn coils (above, below and at the midplane) permitting a maximum current carrying capability of 90 kA-turns with a variety of field spectra possible since each coil has its own power supply. Configurations giving $n < 3$ RMPs were originally deprecated since the field penetrates further as the toroidal mode number decreases, giving rise to concerns about the interaction with intrinsic error fields, inadvertent deleterious effects on the core plasma or even the seeding of locked modes and ensuing disruptions. However, recently low- n RMPs have been used to suppress ELMs in DIII-D ($n = 2$) [21–23] and KSTAR ($n = 1$) [7] without significant degradation of the core performance, opening the question of what the optimal configuration is for ITER.

With its 18 in-vessel coils [24], MAST is able to apply RMPs with toroidal mode numbers $n = 1, 2, 3, 4, 6$, making it ideally suited to investigate the issue of the optimal toroidal mode number for controlling ELMs. In this paper, we document the effect of RMPs in configurations with a range of toroidal mode numbers when applied in MAST and compare with numerical simulations of 3D equilibria and resistive MHD stability. In section 2 the effect of different RMP configurations on the ELM behaviour in MAST is documented, together with an assessment of the effect on the mitigated divertor heat flux. The changes in the plasma configuration, both in terms of lobes near the X-point and the midplane corrugations, due to RMPs with different configurations is outlined in section 3. Section 4 discusses the change in the pedestal structure associated with the RMPs and analyses the stability of the plasma edge for different n_{RMP} . Finally, the toroidal rotation braking, degradation of access to H-mode resultant from RMPs with different periodicities is outlined in section 5. The implications of these various effects for the choice of RMP configuration in ITER is discussed in section 6.

2. Effect of different RMP configurations on ELMs and heat loads

Complete ELM suppression has not been achieved in MAST plasmas, but ELM mitigation—that is to say a marked increase in ELM frequency and commensurate reduction in the divertor peak heat flux per ELM, coming at the price of a drop in plasma confinement—has been achieved with RMPs with a range of toroidal mode numbers in both lower single null diverted (SND) or connected double null diverted (DND) magnetic geometry. It should be noted that for sufficient peak heat flux amelioration, ITER is predicted to require mitigation such that the mitigated ELM frequency is more than 20 times the natural ELM frequency [25], which is a larger increment in frequency than presented in these MAST plasmas. Here, we refer to

the ratio of the mitigated ELM frequency over the natural frequency greater than unity as ‘ELM mitigation’, though it should be remembered that this may not be commensurate with acceptable divertor lifetime in ITER. Figure 1 shows an example of the effect of the application of RMPs with toroidal mode number $n_{\text{RMP}} = 2, 3, 4, 6$ on a SND H-mode plasma with a plasma current $I_p = 400$ kA, an on-axis toroidal magnetic field $B_{T0} = 0.55$ T and an edge safety factor $q_{95} = 3.8$ when heated with 3.6 MW of neutral beam injection (NBI) power. The pedestal collisionality for these MAST plasmas is in the range $\nu_* \in [0.8, 1.5]$. It should be noted that the $n = 1$ locked mode threshold is such that there is no window whereby ELM mitigation is achieved and disruptions are avoided in MAST when $n_{\text{RMP}} = 1$ RMPs are applied. The change in ELM behaviour can be seen from the changes in the D_α emission when the current in the in-vessel coils is applied for different RMP configurations. Also shown is the enhanced particle transport—or so-called density pump-out—that occurs when RMPs are applied as well as the toroidal rotation velocity towards the top of the pedestal. The applied fields with different n_{RMP} reach different magnitudes since for lower- n_{RMP} a back transition to L-mode is triggered at smaller I_{coil} (and correspondingly smaller resonant radial field b_{res}^r), as discussed further in section 5.

The applied resonant field for these different configurations is illustrated in figure 2 for both the same in-vessel coil current and when the coil current is taken from the MAST cases shown in figure 1. The field for these different RMP configurations is calculated using the ERGOS vacuum field line tracing code [26]. The effective radial resonant field component of the applied perturbation normalised to the toroidal field (b_{res}^r) is the amplitude of the resonant Fourier component in the spectrum of b^1 divided by the average value of $\nabla\sqrt{\psi_{\text{pol}}}$ on the magnetic surface, normalised to the major radius [26]:

$$b_{\text{res}}^r = 2 \frac{|b_{m,n}^1|}{R_0 \langle \nabla \sqrt{\psi_{\text{pol}}} \rangle} \quad (1)$$

Near the plasma edge, the $n_{\text{RMP}} = 4, 6$ RMPs give the largest resonant field, with $n_{\text{RMP}} = 2$ giving the weakest resonant field, which should be expected given the current in the in-vessel coils was much lower for the $n_{\text{RMP}} = 2$ case. Indeed, the $n_{\text{RMP}} = 2$ field from the RMPs is of similar magnitude to the intrinsic $n = 2$ error field measured in MAST.

It is possible to vary the effective resonant field at the plasma edge in MAST by varying the current in the in-vessel coils and also by moving the plasma outboard boundary closer towards the coils. Figure 3 shows the ELM frequency normalised to the unmitigated ELM frequency as a function of the radial field calculated with vacuum field line tracing at $\psi_N = 0.98$ for MAST plasmas with $n_{\text{RMP}} = 3, 4, 6$ RMPs applied. Note that the window between the applied field being sufficiently large to affect the ELM behaviour and the field required to induce a back-transition for $n_{\text{RMP}} = 2$ is very small, so we do not include $n_{\text{RMP}} = 2$ in this dataset. It is evident that the ELM frequency increases as a linear function of the applied field provided it is above a critical threshold, which itself is different for the different toroidal mode numbers. The critical b_{res}^r required for ELM mitigation scales with n_{RMP} , with $n_{\text{RMP}} = 3$ being lowest.

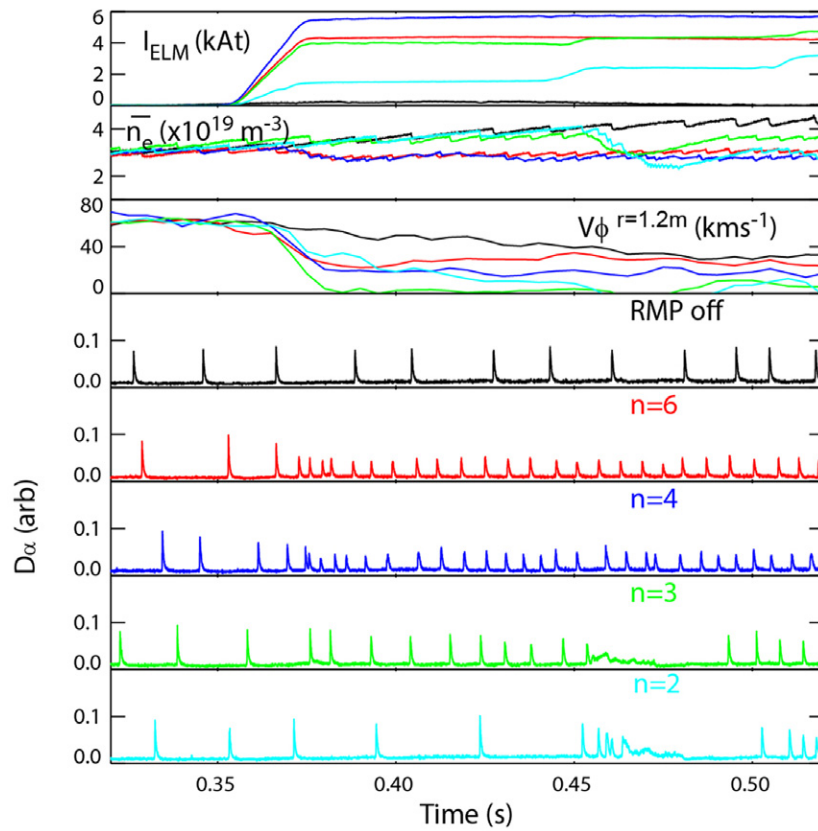


Figure 1. (First pane) the current in the in-vessel coils for different toroidal mode number configurations; (second pane) the line-averaged electron density showing the enhanced particle transport when RMPs are applied; (third pane) the toroidal rotation velocity at $r = 1.2m$ near the plasma edge; (other panes) the D_α emission for the different RMP configurations.

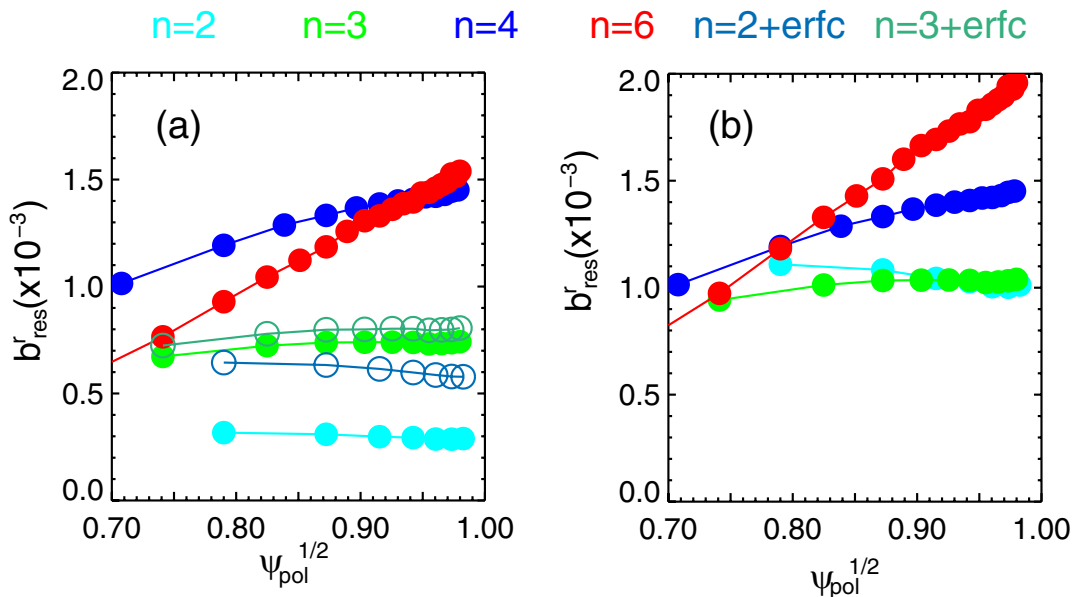


Figure 2. (Left) The radial dependence of the resonant radial field applied from the in-vessel coils in the vacuum approximation as calculated by the *Ergos* code for the RMP configurations with different toroidal mode numbers when the current in the coils is the maximum achievable in the experiment without causing a back-transition, as shown in figure 1. The open symbols are cases with error field correction included. (Right) The resonant fields calculated for the same in-vessel coil currents. The b'_{res} for $n_{RMP} = 6$ is largest since the $n_{RMP} = 6$ applied field is optimally aligned with the equilibrium q -profile nearest to the plasma edge.

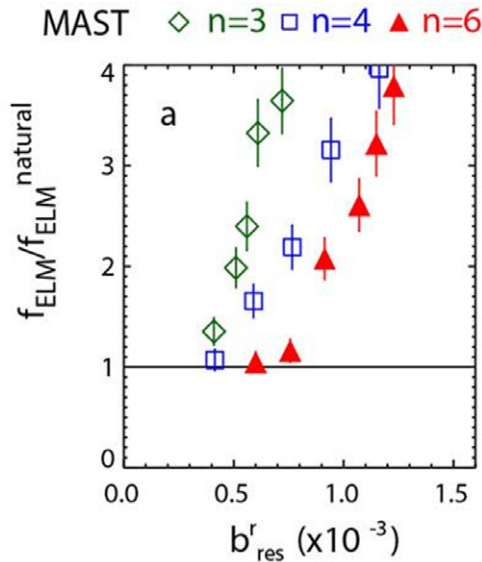


Figure 3. The ELM frequency as a function of the resonant radial magnetic field applied from the in-vessel coils at the nearest rational surface to $\psi_N = 0.98$ calculated with a vacuum approximation. The ELM frequency increases linearly with the applied field above a threshold for all toroidal mode numbers. The threshold in applied field increases with n_{RMP} .

It is observed in MAST that the energy released per ELM, the fractional density loss per ELM and the peak heat flux on the divertor plates decrease as the ELM frequency increases [11]. However, whilst the peak heat flux does scale inverse-linearly with the increasing ELM frequency, there is an offset meaning that as $\Delta W \rightarrow 0$, the peak heat flux remains above the inter-ELM value [33] (where here ΔW is defined as the change in the magnetic energy associated with an ELM as calculated by EFIT). Here we consider the relative merits of the various RMP configurations for mitigating the heat flux on the targets. Figure 4 demonstrates that the peak heat flux to the outer strike point as measured by infrared (IR) thermography scales with the total energy incident on the divertor for RMPs with $n_{RMP} = 3, 4, 6$. This intransigence with RMP periodicity is consistent with the heat flux mitigation resulting from the RMPs reducing the drive for the peeling–ballooning modes, but not changing the nature of the perturbation, that is to say the mitigated ELMs retain their type-I ELM characteristics [11, 12]. The different RMP configurations do lead to different strike point patterns on the targets, as discussed later in section 3, but do not affect the peak heat flux resultant from the mitigated ELMs. The reduction in peak heat flux is observed to scale with the ΔW_{DIV} for all cases of n_{RMP} .

Whilst lower peak heat flux is shown in figure 4 for $n_{RMP} = 4, 6$ than $n_{RMP} = 3$, this is simply because the ELM frequency is lower in these $n_{RMP} = 3$ shots for the level of applied field, since the b_{res}^r is lower (see figure 2). Since the avoidance of damage to in-vessel plasma facing components is the primary motivation for the application of RMPs, if one configuration leads to optimal peak heat flux mitigation, this would almost certainly result in that configuration being used. However, since that is not the case, the choice of optimal RMP configuration in ITER will relate to the second order effects discussed in the following sections.

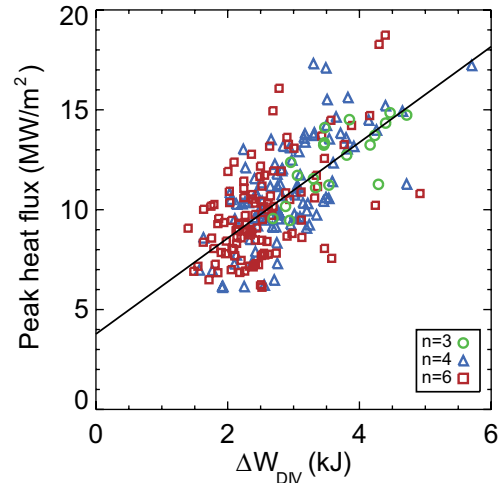


Figure 4. The peak heat flux to the outer strike point measured by IR thermography as a function of the total energy to the divertor for different RMP configurations.

3. Effect of different RMP configurations on plasma configurations

3.1. Lobes near the X-point

When non-axisymmetric fields are applied, the resultant tangled magnetic fields are predicted to lead to the formation of lobe structures near the X-point [27]. Such structures have been directly observed in MAST [10, 28] and DIII-D [29], and used to explain the splitting of the divertor leg footprints observed on strike-point targets in various experiments with RMPs (see for instance [30–32]). The lobe structures have very different characteristics depending on the configuration of the RMP applied. Figure 5 shows images of the plasma in the vicinity of the lower X-point for $n_{RMP} = 3, 4, 6$ in MAST single-null plasmas (as shown in figure 1) as measured by the filtered visible-imaging camera. The 3D location in the vessel where the camera viewing chords are tangent to toroidal surfaces are calculated using a ray tracing code. It is assumed that the majority of the light detected at a given pixel originated in close proximity to this tangency position, in order to localise the measurement. Unperturbed equilibrium flux surfaces are mapped to each pixel's tangency location, allowing the image to be mapped in terms of normalised flux. For pixels whose viewing chords are approximately tangential to the edge of the plasma, it can be assumed that the light detected at a given pixel originated in close proximity to the tangency position. For all n_{RMP} , the radial extent of the lobes increases linearly with the resonant field applied [28]. The lobes resultant from the application of higher- n_{RMP} RMPs have narrower poloidal extent, but increased radial extent.

Figure 6 shows the images from 5 mapped to the equilibrium toroidal flux for RMPs with the same b_{res}^r . The apparent size of a lobe is measured by examining the variation of the He^{1+} light emitted from the plasma as a function of the distance from the separatrix, at a given poloidal angle [28]. The camera data is interpolated onto a regular mesh of poloidal angle and radial distance from the last closed flux surface

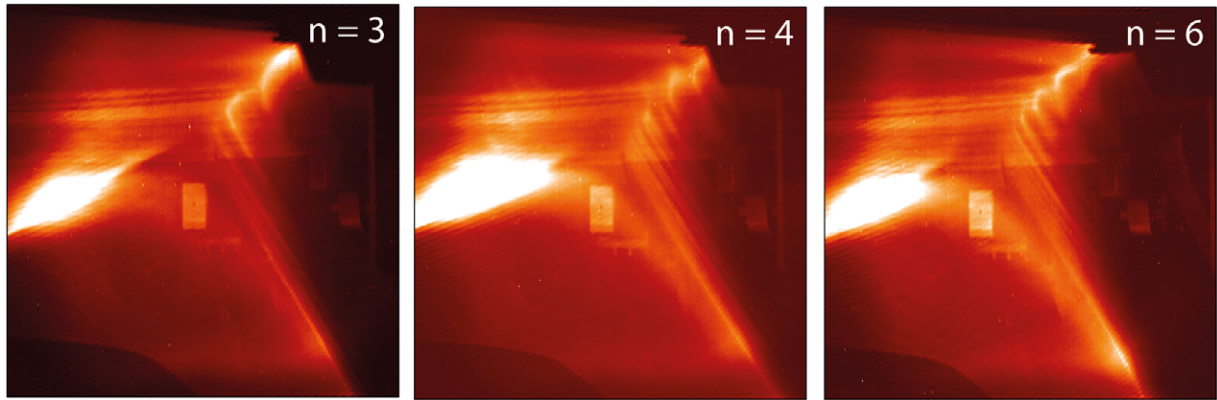


Figure 5. Filtered visible imaging of C2+ (465 nm) light from the plasma in the vicinity of the X-point when (left) $n_{\text{RMP}} = 3$ with $I_{\text{coil}} = 5$ kAt (centre) $n_{\text{RMP}} = 4$ with $I_{\text{coil}} = 5.6$ kAt, (right) $n_{\text{RMP}} = 6$ with $I_{\text{coil}} = 5.6$ kAt RMPs are applied.

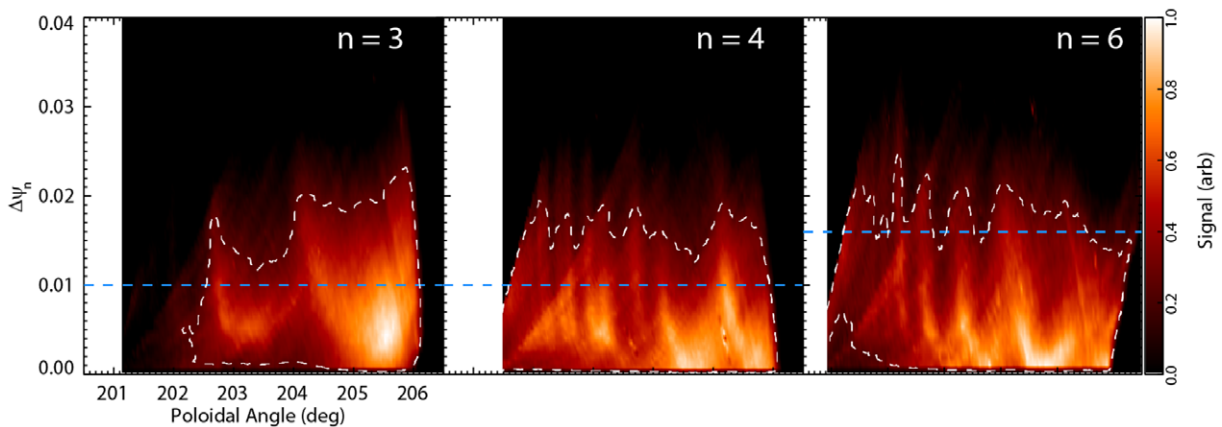


Figure 6. The camera images shown in figure 5 mapped as a function of poloidal angle and equilibrium flux. The blue dotted lines illustrate where the light detected by the camera fell to half of the peak value near the separatrix, before the RMP was applied but the plasma was still in H-mode. Note that the $n_{\text{RMP}} = 6$ case has slightly more input power, meaning that the edge is slightly hotter so the region of the SOL which emits C²⁺ light will be slightly extended, but nonetheless, the longer lobes are consistent with field line tracing [28].

for analysis purposes. It is clear that the size of the lobes—defined to be the distance over which the light intensity falls to 1/3 of its peak (separatrix) value—varies with n_{RMP} , with the lobes being longest when an $n_{\text{RMP}} = 6$ field is applied. The approximate location of the plasma boundary, measured where the C²⁺ light intensity falls to 1/3 of its peak value prior to the application of an RMP, is indicated by a blue dashed line. The $n_{\text{RMP}} = 6$ lobes data was collected from a pulse with stronger NBI heating, which resulted in an increase in the edge electron temperature. As C²⁺ light emission is highly sensitive to electron temperature, this resulted in the apparent edge of the plasma moving deeper into the scrape-off layer (SOL).

3.2. Corrugation at the midplane

As well as giving rise to lobe structures near the X-point, the application of RMPs in MAST also gives rise to a toroidal corrugation of the plasma midplane [24, 34, 35]. These displacements have been measured in MAST double null configuration with $n_{\text{RMP}} = 3$ and $n_{\text{RMP}} = 4$ RMPs applied (with $n_{\text{RMP}} = 6$ leading to negligible displacement in a double null configuration since the plasma is too far from the lower set

of coils used to create an $n_{\text{RMP}} = 6$ field). We use double-null plasmas in this section of the paper (compared to the single-null plasmas elsewhere) since MAST has a number of diagnostics capable of measuring the plasma boundary with sub-cm radial resolution at the midplane located in various toroidal sectors around the vessel. This allows a toroidal map of the boundary position to be measured for different phases of applied field [24]. Reference [34] shows the midplane boundary position as a function of the toroidal angle when $n_{\text{RMP}} = 3$ and $n_{\text{RMP}} = 4$ RMPs are applied respectively. The boundary corrugations are measured by the Thomson scattering diagnostic, visible imaging cameras, a linear D_α camera, the charge exchange recombination spectroscopy diagnostic and an RGB camera. Here, the displacement is inferred from measurements of different quantities using different diagnostics. For instance, in order to find the displacement associated with the RMPs using the Thomson scattering diagnostic, firstly modified tanh fits are made of the data for time points just before an ELM, with the displacement described by the difference between the radial position of an isotherm with and without RMPs applied. Similar methods for assessing the radial excursion of a surface at which the different measured variables are constant allow inference of the displacement at

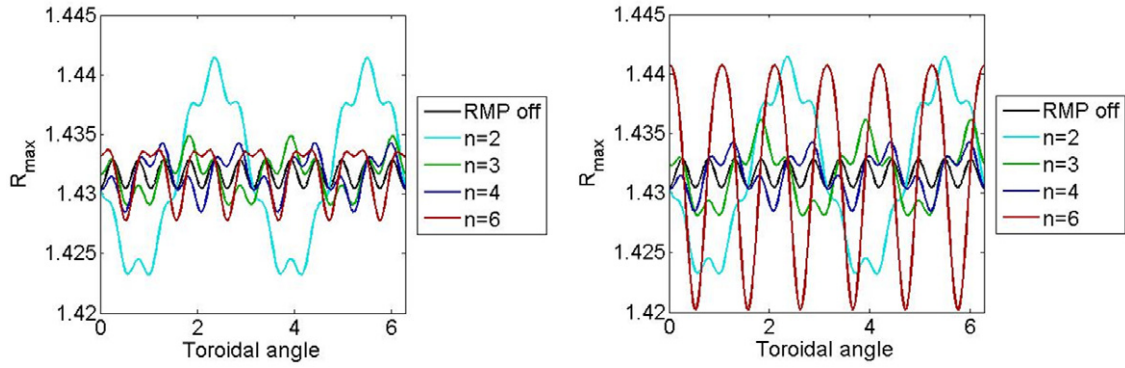


Figure 7. The radial position of the plasma boundary at the outboard midplane as a function of toroidal angle as predicted by VMEC when $n_{\text{RMP}} = 2, 3, 4, 6$ RMPs are applied at (left) full field and (right) scaled such that b'_{res} is the same at the separatrix. The displacement associated with the $n = 12$ toroidal field ripple is included here.

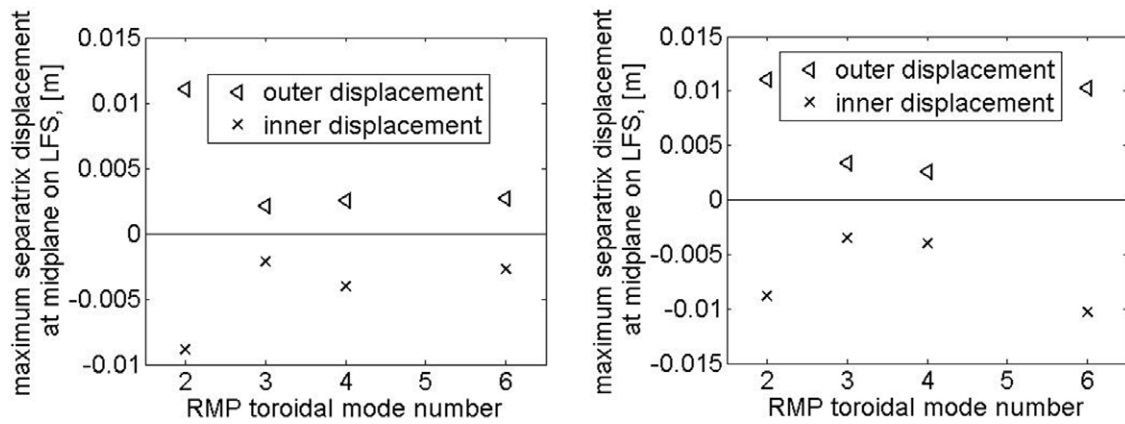


Figure 8. The maximum corrugation inward and outward compared to the separatrix without an applied RMP as calculated by VMEC for different n_{RMP} applied at (left) full field and (right) scaled such that b'_{res} is the same at the separatrix. The RMP configurations are the same as shown in figure 7.

different toroidal angles, as described in detail in [24]. Upon application of the RMPs, the plasma boundary experiences a toroidal corrugation with periodicity and phase dictated by the applied non-axisymmetric field. For both the $n_{\text{RMP}} = 3$ and $n_{\text{RMP}} = 4$ RMPs, the displacement of the boundary is of the order of ± 2 cm, equivalent to $\pm 4\%$ of the minor radius [34].

The displacements have been shown to be in good accordance with those predicted by a 3D equilibrium reconstruction using the VMEC code [24]. VMEC is a code which calculates equilibria without the assumption of axisymmetry. In general there is no non-axisymmetric analogue of the Grad-Shafranov so the technique of energy minimization is used with the assumption of nested flux surfaces. The free boundary version of the code allows the locations of the RMP coils to be included in the description of the vacuum magnetic field. The non-axisymmetric equilibrium is then calculated. The plasma is in force balance with the RMPs applied. The plasma response is effectively the non-linear, fully penetrated, ideal plasma response. The nested flux surface assumption means that no islands form as a result of the RMPs. Accordingly, we have used VMEC to predict the midplane corrugation amplitude for a range of n_{RMP} and b'_{res} . Figure 7 shows the position of the plasma boundary as a function of toroidal angle predicted by VMEC when

$n_{\text{RMP}} = 2, 3, 4, 6$ RMPs are applied in a MAST double-null plasma for the case with full current in the in-vessel coils, and for a case with matched b'_{res} at the plasma boundary. It is evident that for the same applied current in the in-vessel coils, the lower- n_{RMP} fields lead to a larger distortion of the plasma boundary at the midplane. However, since the field decays faster for higher- n_{RMP} (which is particularly important for double null plasmas which are geometrically located further from the in-vessel coils [11]), when the resonant field at the boundary is the same, the corrugation caused by $n_{\text{RMP}} = 6$ is exacerbated. Figure 8 shows the maximum corrugation for each RMP configuration, again for both the case with full current in the in-vessel coils, and for a case with matched b'_{res} at the plasma boundary. It is evident that the $n_{\text{RMP}} = 2, 6$ cases lead to the largest maximum corrugation. Note that here the $n_{\text{RMP}} = 3$ field is produced by powering alternate coils (+0-0+0-0-0) whereas the $n_{\text{RMP}} = 4$ field uses all twelve coils in the lower row (++-+-+--+). Since there are more coils energised for the dominantly $n_{\text{RMP}} = 4$ case, the field does not need to be scaled proportionately with n_{RMP} .

Whilst the predictions from an ideal 3D equilibrium code such as VMEC have replicated the measured displacements in MAST [24, 35], the code assumes nested flux surfaces. Since the lobe structures near the lower divertor illustrated in figure 5 are consistent with field line reconnection, we

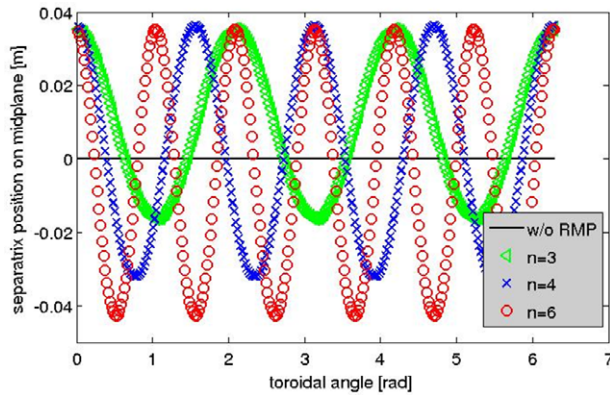


Figure 9. A toroidal map of the separatrix position predicted by JOREK when $n_{\text{RMP}} = 3, 4, 6$ RMPs are applied in MAST for the same in-vessel coil current, compared to the separatrix location without an applied field.

have also applied a resistive MHD model to consider the boundary displacements. Here the JOREK nonlinear MHD code [40] is run with single toroidal mode number and a non-axisymmetric field applied until it reaches saturation as a new equilibrium state [41]. The toroidal mode number corresponds to the toroidal mode of the RMP configuration ($n = 3, 4$ or 6). We do not retain the higher- n harmonics in these simulations to avoid any ELM-related perturbations, so that only the RMP perturbation with mode $n = 3, 4$ or 6 is obtained. Any non-linear coupling between the applied field and higher- n modes is thus neglected. We consider a double-null MAST configuration making use of the double null geometry developed in [42]. The RMP field is ramped up over 20 ms. The plasma resistivity in JOREK is assumed to be $\eta = 6 \times 10^{-6} \Omega \text{m}$ —approximately 300 times larger than in MAST—with perpendicular (parallel) viscosity of $\mu_{\perp} (\mu_{\parallel}) = 3 \times 10^{-6} (3 \times 10^{-5}) \text{kg m}^{-1} \text{s}^{-1}$, and a Lundquist number of $S = 2.21 \times 10^5$. In previous studies of ELMs in MAST with the JOREK code [42], it was found that ELM filament dynamics, energy losses, and divertor heat fluxes, were best reproduced simultaneously with a higher resistivity than experimental values. The choice of such high resistivity and its effect on ELMs is discussed in that paper. The aim of the simulations presented here was to produce RMP modelling in an ELM-unstable plasma, hence the same base case with high resistivity, as in [42], was chosen for these simulations. The effect of resistivity on RMP penetration/screening will be studied in more details in the near future, the effort here being focused on the difference between modes $n_{\text{RMP}} = 3, 4$ and 6 . We let the electric field evolve according to the MHD equations and the plasma pressure. No electric field is imposed in the simulation. In order to obtain a transport barrier in the pedestal, the perpendicular diffusivity is reduced by a factor 10, as described in [42].

Figure 9 shows the position of the separatrix as predicted by JOREK as a function of toroidal angle for MAST double-null plasmas with saturated $n_{\text{RMP}} = 3, 4, 6$ fields compared to the separatrix position without a non-axisymmetric field applied. The midplane displacement is of the order of ± 2.5 cm, in good agreement with the measured displacements. Figure 10 shows the maximum corrugation predicted by JOREK for different RMP configurations. In agreement

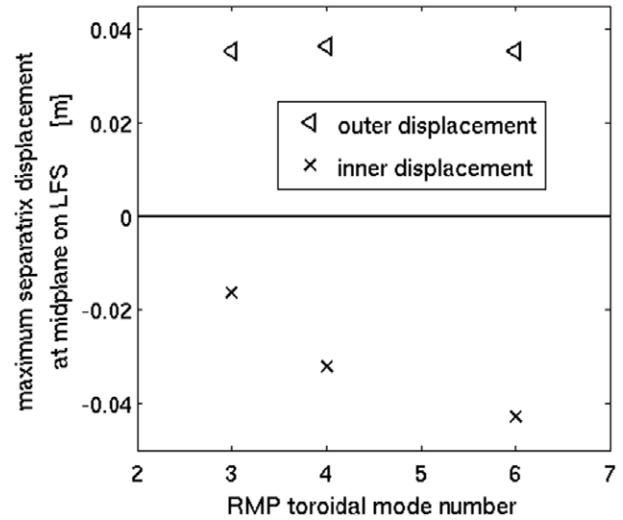


Figure 10. The maximum corrugation inward and outward compared to the separatrix position without RMP applied calculated by JOREK when $n_{\text{RMP}} = 3, 4, 6$ RMPs are applied in MAST for the same in-vessel coil current. The RMP configurations are the same as shown in figure 9.

with the VMEC simulations shown in figure 8, the largest corrugation occurs for $n_{\text{RMP}} = 6$.

4. Effect of different RMP configurations on the pedestal and edge stability

4.1. Pedestal structure

When an $n_{\text{RMP}} = 6$ RMP with 0° phase is applied, Thomson scattering measurements show a drop in density pedestal height as well as increase in both density and temperature pedestal width [36]. The three-dimensional (3D) nature of the profiles has been investigated in these MAST plasmas by comparing the pedestal profile measured by the Thomson scattering diagnostic with linear D_α camera measurements in an adjacent MAST sector (ie approximately 30° out of phase). ERGOS predicts that the boundary perturbation upon application of an $n_{\text{RMP}} = 6$ with 0° phase ($n_{\text{RMP}} = 6$ with 30° phase) RMP will be maximum (minimum) when measured by the Thomson scattering diagnostic and correspondingly minimum (maximum) when measured by the linear D_α camera. The measurements of density gradient as a function of radius from these two diagnostics are shown in figure 11. Here, the D_α emissivity is obtained from spatial inversion of line of sight integrated intensity D_α profiles as measured by a linear camera. The radial D_α emissivity profile is a product of the of the neutral and electron densities and of the rate co-efficient for populating the $n = 3$ principal quantum level. Under certain assumptions, as detailed in [37], a simple relationship may be obtained between the density gradient, neutral influx velocity and D_α emissivity profile width. The neutral influx velocity is obtained as a free parameter fit to electron density gradients as measured by the Thomson scattering at low density gradient. There are a number of possible systematic errors in this method of measurement, however, relative changes in gradients over similar shots should be accurate. Although the absolute value of the gradient differs from the Thomson scattering gradient,

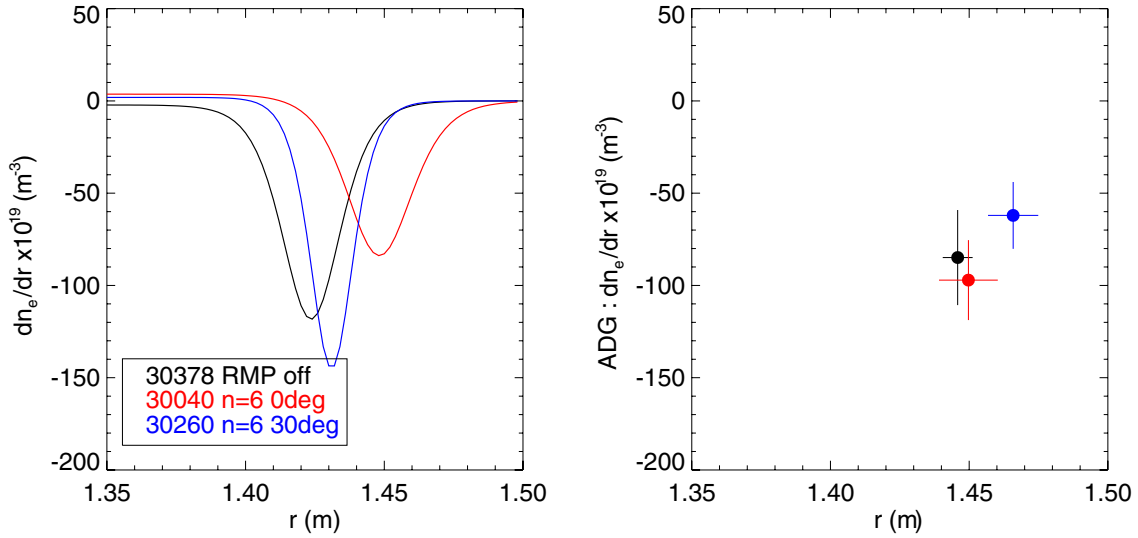


Figure 11. The radial profile of the electron density gradient as measured by (left) the Thomson scattering diagnostic and (right) the D_α camera in MAST with and without an $n_{\text{RMP}} = 6$ RMP applied.

the relative variation of gradient levels is found to be consistent for shots with no applied RMP. The Thomson scattering shows that the pedestal width increases and location moves outward for the $n_{\text{RMP}} = 6$ 0° RMP, whilst the linear D_α data shows that the peak gradient location does not move and the density gradient magnitude shows a slight increase. Conversely, with an $n_{\text{RMP}} = 6$ 30° RMP field, the linear camera measures the peak gradient to decrease strongly and move outwards by ~ 20 mm whilst the Thomson scattering observes negligible change in the position of the pedestal but an increase in the density gradient. On application of the $n_{\text{RMP}} = 6$ RMP, the edge locations observed by the D_α emission and the Thomson scattering move in opposite directions with respect to one another. However, due to the complicated edge position feedback, it cannot be excluded that there is an absolute change in edge location. That is to say in figure 11, the mean separatrix location could be different on application of the RMP. The purpose of this figure is to illustrate that the density gradient is also toroidally varying. The effect of the radial position control when RMPs are applied is discussed in more detail in [35]. Since there is a density pedestal height drop on application of RMP, the density width is contracting to cause an increase in gradient. No change in pedestal width has been observed from examination of the profiles on the high field side when RMPs are applied. This indicates toroidally varying density pedestal width, and hence toroidally varying pressure gradients on the low field side when non-axisymmetric fields are applied, indicating the importance of performing stability calculations based upon a 3D equilibrium.

This toroidal variation of the pressure gradient is present upon application of all mode numbers of RMP. Figure 12 shows the degradation of the pedestal height and increase in the pedestal width for $n_{\text{RMP}} = 3, 4, 6$ for plasmas with very similar b'_{res} . This degradation in the pedestal density is also observed in JOREK resistive MHD modelling, where the RMPs cause enhanced particle transport and a decrease in pedestal pressure, for all n_{RMP} , as seen in figure 13. Whilst the simulations qualitatively observe the density pump-out as seen experimentally, a quantitative comparison with

experiment will require a better match between the JOREK parameters and the experiment. In JOREK the enhanced particle transport results from both convective cells [38] and magnetic field stochasticity, thus both density and temperature are lost, contrary to the experimental observations where the temperature is largely unperturbed. The degradation of the pedestal height is similar for all n_{RMP} , and in all cases, the pedestal pressure can be largely recovered by refuelling the plasma to counter the enhanced particle transport incurred by the RMP fields [39].

The evolution of the pedestal in mid-collisionality plasmas ($v_e^* \in [0.8, 1.5]$) such as those presented here has been attributed to mediation by kinetic ballooning modes limiting the pedestal gradient until the pedestal width increases to the point at which finite- n ballooning modes become unstable [43]. Infinite- n ballooning stability has been compared to gyrokinetic analysis for MAST plasmas without RMPs and shown to be a good proxy for kinetic ballooning mode stability [43]. Here we use the VMEC code [44] to generate non-axisymmetric equilibria for MAST plasmas with $n_{\text{RMP}} = 2, 3, 4, 6$ applied and then find the $n = \infty$ ballooning mode growth rate using the COBRA code [45] to compare to the pedestal structure shown in figure 12. Figure 14 shows the $n = \infty$ ballooning mode growth rate—as a proxy for kinetic ballooning mode stability—across the radial extent of the pedestal. Here, the growth rate is shown for a toroidal position where instability is exacerbated, though in a different toroidal phase the $n = \infty$ growth rate is decreased relative to the case without RMPs [57]. The non-axisymmetric perturbation of the pedestal exacerbates kinetic ballooning mode instability, widening the region over which infinite- n modes are unstable and enhancing the mode growth rate. Assuming infinite- n modes remain a good proxy for kinetic ballooning modes, this suggests that particle transport, assuming a crude gyro-Bohm diffusivity scaling like γ/k^2 (where γ is the growth rate and k is the perpendicular wavenumber), is enhanced, consequently limiting the pressure gradient to a lower value. This is consistent with the pedestal width increasing locally in

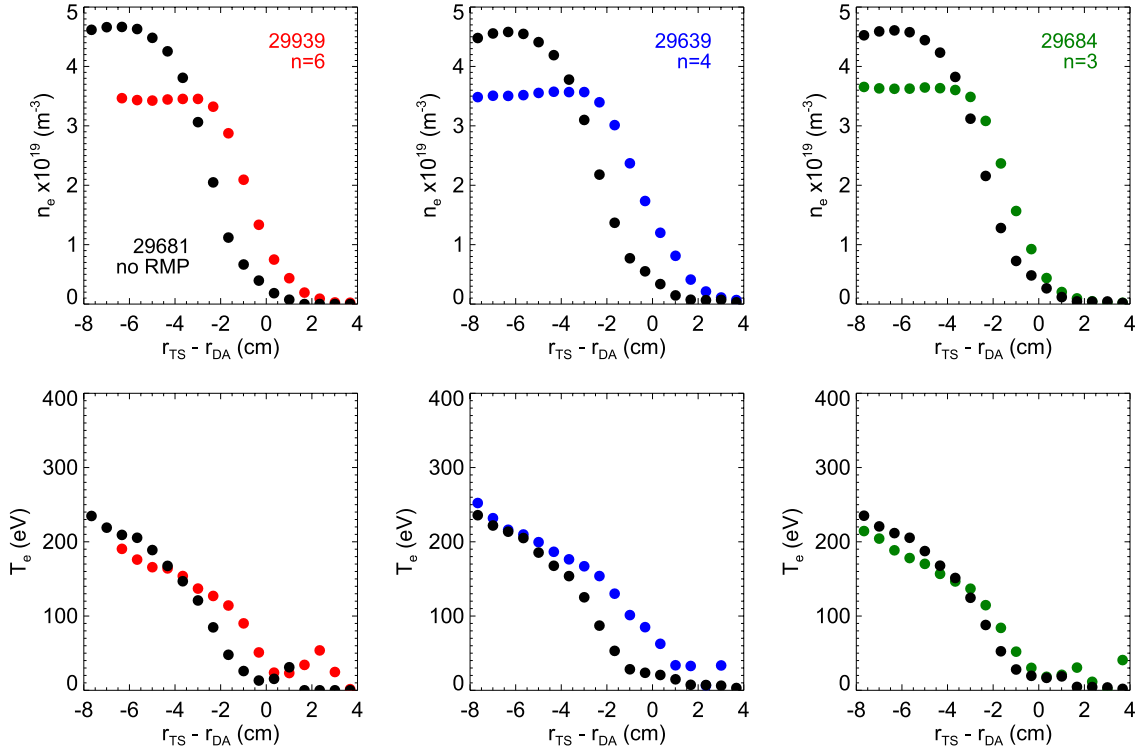


Figure 12. The electron density and temperature measured by the Thomson scattering at the end of the ELM cycle in a shot without RMPs compared to the profiles with $n_{RMP} = 3, 4, 6$ applied averaged over multiple ELMs. The time-windows over which the with and without RMP cases are averaged is different for each n_{RMP} , explaining why the profiles without RMPs change slightly.

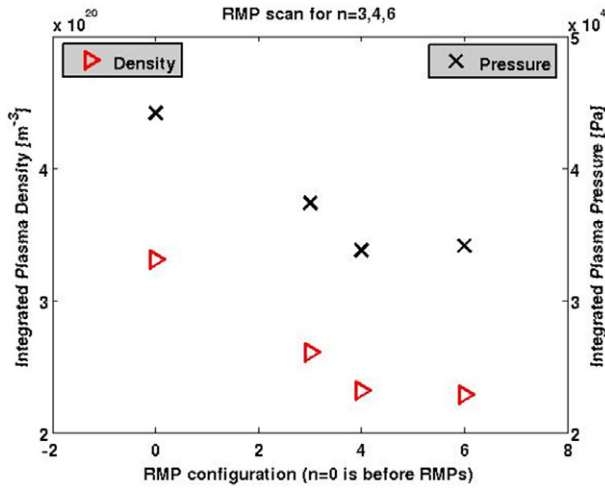


Figure 13. The pedestal density and pressure height as calculated by JOREK for a 3D equilibrium when $n_{RMP} = 3, 4, 6$ RMPs are applied.

the most unstable toroidal position before the finite- n peeling–ballooning limit is reached after the application of RMPs, as observed empirically in figure 11. The region over which the infinite- n ballooning modes become unstable, and the enhancement in their growth rate, is similar for all RMP configurations, consistent with the pedestal structure being similar for all n_{RMP} . When an $n_{RMP} = 3$ field is applied, the pedestal pressure must be reduced by 30% for the infinite- n ballooning mode growth rate in the toroidal position of greatest instability to equal that in the case with no RMPs [57]. The

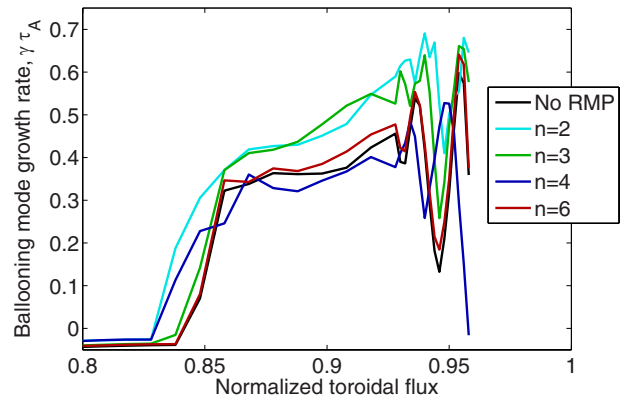


Figure 14. The $n = \infty$ ballooning mode growth rate as a function of radius across the pedestal region for a single null plasma with no RMPs compared to cases with full field applied in $n_{RMP} = 2, 3, 4, 6$ configurations. The radial extent of the region of positive ballooning mode growth rate shows a clear increase in the cases where the plasma displacement is largest, commensurate with the increase in pedestal width observed.

reduction in the pedestal pressure to reach marginal stability may be different for other RMP mode numbers [57].

5. Other effects of different RMP configurations on the plasma

5.1. Toroidal plasma rotation braking

The toroidal rotation of the plasma is observed to decrease across the whole plasma minor radius when the RMPs are

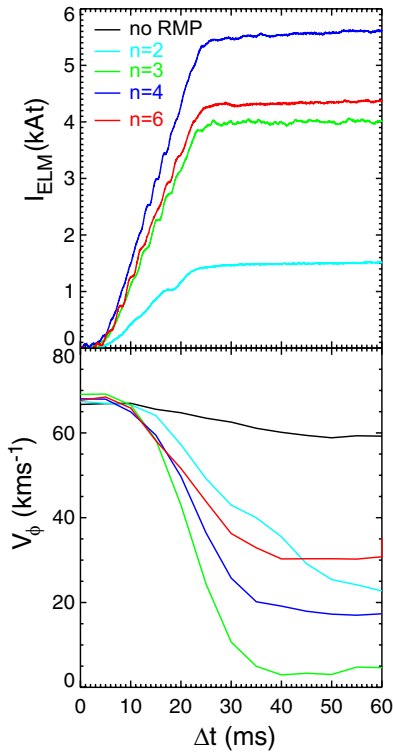


Figure 15. The rotation frequency as measured by the charge exchange spectroscopy in MAST at $\psi_N = 0.3$ as a function of time. Also shown is the current in the in-vessel coils, which is lower amplitude for low- n_{RMP} to avoid plasma locking causing an H–L transition.

applied to single null discharges, such as those shown in figure 1. Braking occurs for all RMP configurations, though it is so severe for $n_{\text{RMP}} = 2, 3$ it causes a back transition before the current in the in-vessel coils reaches its maximum value (at least for the q_{95} and proximity to the in-vessel coils of the plasma studied here). Figure 15 shows the toroidal rotation measured by charge exchange recombination spectroscopy at a radial position just inside the top of the pedestal as a function of time. Also shown is the waveform of the in-vessel coil currents, illustrating that different maximum field amplitudes are applied since the braking is so severe for low- n_{RMP} as to cause loss of H-mode. The plasma rotation decreases slightly even in the absence of applied RMPs, likely to be due to the torques associated with intrinsic error fields [46]. The deceleration is approximately the same for all RMP configurations, though the saturated level depends on n_{RMP} . The braking is strongest for $n_{\text{RMP}} = 2$, noting that the applied field is only a third as large as other configurations to preclude a back-transition. $n_{\text{RMP}} = 3$ induces the next strongest braking torque, with $n_{\text{RMP}} = 4, 6$ producing a similar braking and saturating at finite rotation. Here we assume that if the applied field with $n_{\text{RMP}} = 2$ had been stronger then the rotation braking would be commensurately increased, as observed in MARS-Q simulations described below.

Figure 16 shows the time evolution of the plasma rotation at different rational surfaces in these MAST single null plasmas. In all cases there is global plasma braking across the whole of the minor radius, with the braking being strongest for lower- n_{RMP} fields.

The effect of RMPs on the plasma flow has been simulated using the quasi-linear MARS-Q code [47]. MARS-Q solves the full MHD, single-fluid equations to find the plasma response in full toroidal geometry. These perturbed MHD equations are then coupled to the momentum balance equation for the change in the toroidal flow of the plasma and solved using a semi-implicit adaptive time-stepping scheme nonlinearly in time. The model incorporates both the NTV torque [50] and the $j \times B$ torque [49] with both resonant and non-resonant contributions included. A thorough description of the model and the nonlinear evolution of the contributions from these different torques when RMPs are applied in MAST can be found in [47]. To simulate the MAST plasmas shown in figure 16, a resistive plasma model is assumed with magnetic Lundquist number $S_0 = 3.5 \times 10^7$ at the magnetic axis, with a profile given by $S \sim T_e^{3/2}$, so $S_{\text{edge}} \approx 10^6$. The non-axisymmetric field is ramped up over 20 ms, as done experimentally, and the intrinsic error field is included for the $n_{\text{RMP}} = 2$ case. It is evident that a similar braking is replicated near the plasma edge for the higher- m rational surfaces. Whilst the deceleration is similar in the core plasma, the saturated rotation level is higher numerically than observed in MAST.

The rotation braking predicted by MARS-Q in these plasmas is less than in other single null MAST discharges—for instance, those reported in higher-current plasmas in [11, 47, 51]—thought to be due to the initial rotation profile. These simulations begin with an initial rotation profile with slower edge velocity matching the conditions in the experiment, presumably due to enhanced fast ion losses at lower current giving rise to counter-current fast particle driven $j \times B$ torques [48]. The braking associated with the RMPs is equally due to the NTV and $j \times B$ torques, whereas the braking in the case with a faster edge rotation is dominated by $j \times B$ torque. Increasing the momentum diffusivity does not lead to an increase in the core braking, with the simulations proving more sensitive to the initial rotation profile. Nonetheless, the edge rotation braking predicted by MARS-Q agrees very well, both in amplitude and deceleration, with observations from MAST (figure 17).

5.2. Degradation of access to H-mode

Dedicated experiments have been performed to assess the implications of applying RMPs in $n_{\text{RMP}} = 2, 3, 4, 6$ configurations on the power required to access high confinement mode. The RMPs are applied before the time at which the L–H transition occurs in a discharge with no applied field. The discharge shown in figure 18 has 5.6 kAt of current in each of the RMP coils and 1.5 MW of beam power. Applying 0.5 MW of beam power is sufficient to cause an L–H transition when no RMPs are applied, hence these discharges are significantly above the no-RMP L–H transition power threshold. The shots are in density feedback, maintaining the density at the transition time taken from the no applied RMP discharge. Without this feedback, the particle pumpout caused by the RMPs prevents H-mode access due to changes in the density dependent power threshold. The application of $n_{\text{RMP}} = 3$ and $n_{\text{RMP}} = 4$ RMP in figure 18 cause a short delay of the L–H transition time of approximately one energy confinement time. The application of $n_{\text{RMP}} = 6$ also results in

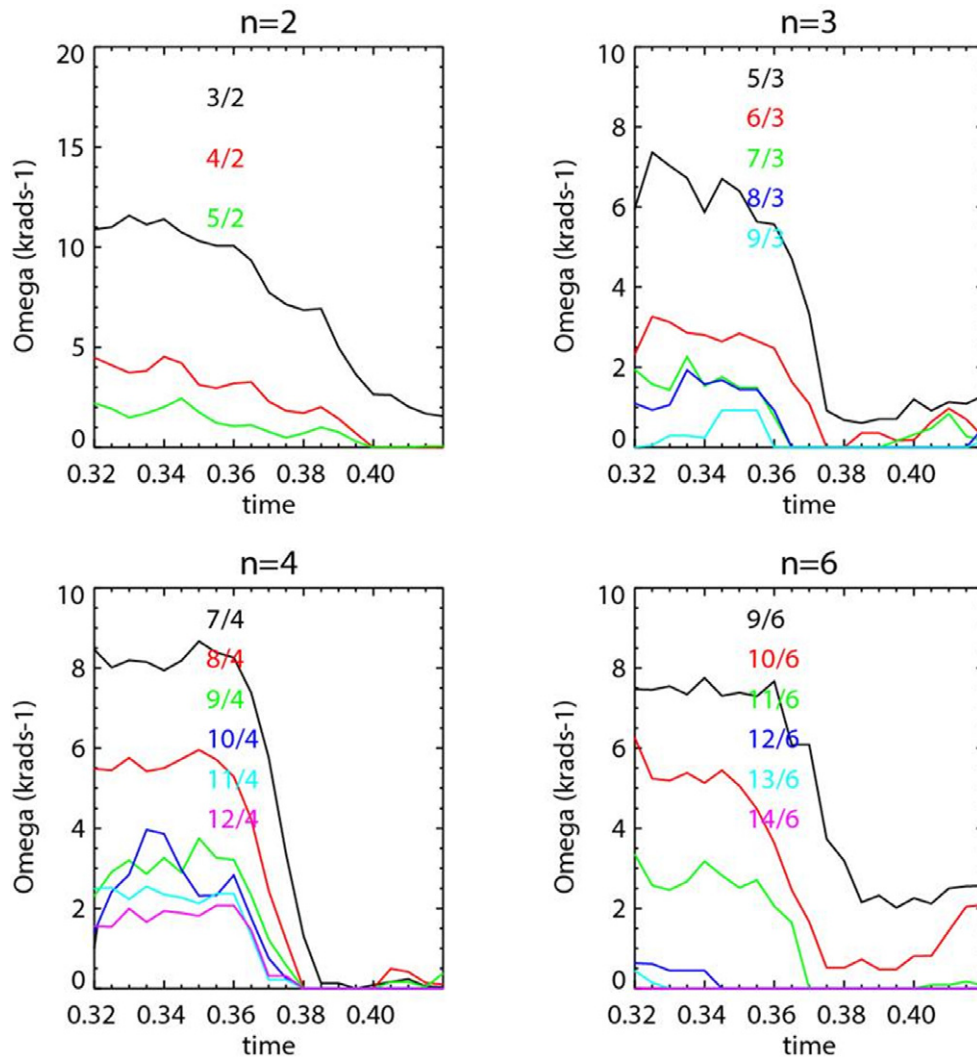


Figure 16. The rotation frequency as measured by the charge exchange spectroscopy in MAST at different rational surfaces when $n_{\text{RMP}} = 2, 3, 4, 6$ RMPs are applied in single-null plasmas shown in figure 15.

a delayed transition, although the delay is significantly longer. The magnitude of the applied RMP field in this case is sufficient to cause an approximate doubling of the ELM frequency in the $n_{\text{RMP}} = 3, 4$ and 6 cases. At the same RMP coil current level, the application of $n_{\text{RMP}} = 2$ RMPs causes a complete suppression of the transition. These results suggest that the power required to access H-mode is non-monotonic with n_{RMP} and is optimal for an RMP configuration with $n_{\text{RMP}} = 3$ or 4 in MAST. It is not yet understood why the power required to access H-mode is lowest for these configurations. The density and temperature profiles for the different RMPs show very little difference before the L–H transition, though there are demonstrable differences in the plasma rotation, suggesting that a modification of the radial electric field by the RMPs could cause the variation in the L–H power threshold.

6. Discussion and conclusions

The MAST experiments and numerical modelling presented here has focussed on the effects of RMPs on various plasma parameters when different RMP configurations are

applied. The in-vessel coil set planned for ITER has 27 coils with individual power supplies, meaning that there is significant flexibility in the system to optimise the periodicity of the applied field, with $n_{\text{RMP}} = 3$ or 4 the anticipated configurations. Since the primary purpose of the in-vessel coils is to mitigate the ELM heat flux sufficiently to ensure an adequate lifetime of plasma facing components, if there were an RMP configuration which maximised the peak heat flux reduction, this would be the major consideration.

In MAST, an increase in ELM frequency has been achieved across a wide range of pedestal collisionalities, including those for which other experiments have observed ELM suppression [6, 7]. For these plasmas with mitigated type-I ELMs, the peak heat flux scales with the ELM frequency, with the different RMP configurations all exhibiting this linear relationship. Consequently, a configuration which maximises the ELM frequency will mitigate the peak heat flux most effectively. Since various RMP periodicities are predicted to meet the empirical conditions for ELM suppression in ITER [16], it is likely that, notwithstanding the uncertainties in the understanding of RMP ELM suppression which negate reliable

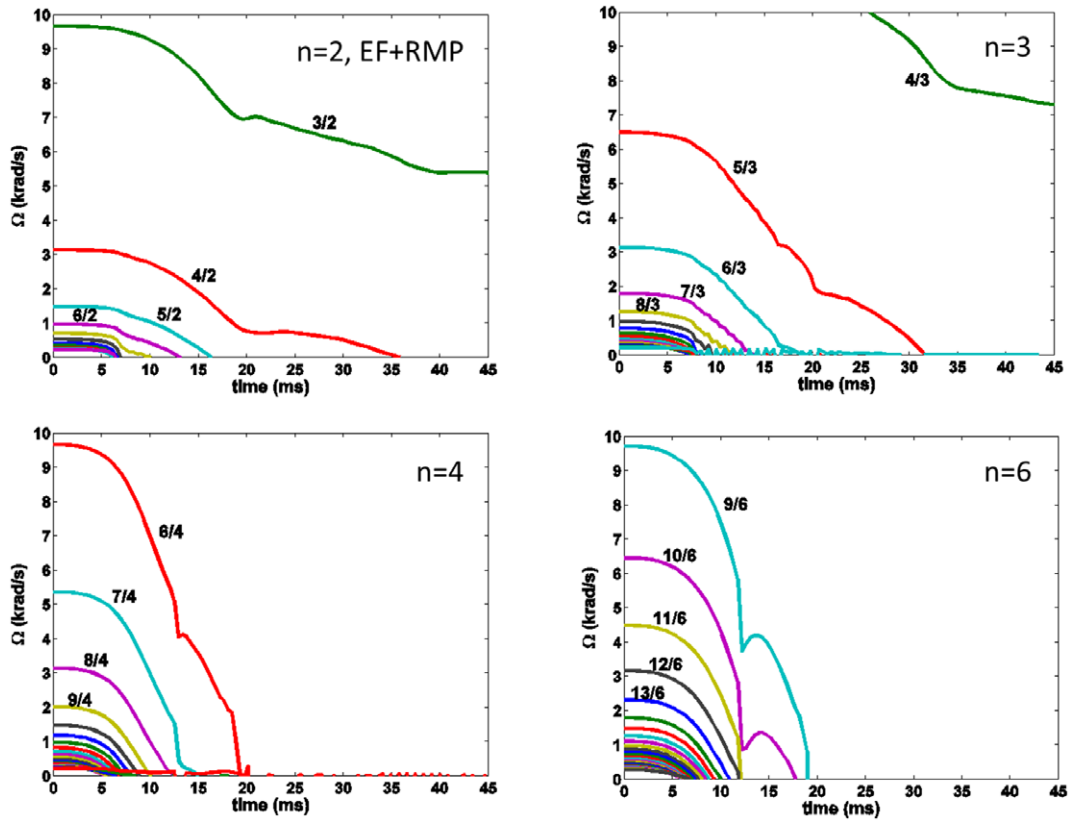


Figure 17. The toroidal rotation frequency at various rational surfaces as a function of time as predicted by MARS-Q simulations of the MAST plasmas shown in figure 16.

extrapolation, an increase in ELM frequency will be possible. Indeed, an increase in ELM frequency has been achieved in all machines, and over a much wider parameter space than ELM suppression [54]. Figure 3 shows that above a threshold value, the ELM frequency, and hence the reduction in peak heat flux, scales linearly with the applied field. This relationship between the applied field amplitude and the mitigated ELM frequency is often observed [54]. The fact that the threshold value for an increase in the ELM frequency scales with n_{RMP} in MAST suggests that $n_{\text{RMP}} = 3$ is more likely to achieve a requisite level of ELM mitigation in ITER than $n_{\text{RMP}} = 4$ or 6. The b_{res}^r threshold value for an increase in the ELM frequency extrapolated from current devices is considerably lower than the achievable value in ITER. It should be noted that this is purely empirical conclusion only from MAST, and consequently the choice of optimal RMP configuration may be determined by other factors; a summary of the optimal configurations for these other physical metrics in MAST is given in table 1.

It is evident that $n_{\text{RMP}} = 2$ at sufficient amplitude to mitigate the ELM heat flux has the most detrimental effect on these MAST plasmas. Conversely, RMPs with periodicity $n_{\text{RMP}} = 3, 4$ have least deleterious side-effects on the plasma when mitigating ELMs. Whilst $n_{\text{RMP}} = 4$ has a higher locked mode threshold, $n_{\text{RMP}} = 3$ has a lower critical field for increasing the ELM frequency, which means that less applied field is required to achieve the same reduction in peak heat flux. $n_{\text{RMP}} = 4$ RMPs also have the advantage of causing least degradation to the power threshold required to access H-mode. Whilst $n_{\text{RMP}} = 3$ cause less radially extended lobe structure

near the X-point, they are more poloidally extended, so may interact more with the first wall.

The reasonable agreement between numerical modelling with MAST data for rotation braking, 3D corrugation and lobe structures shown in this paper suggests that these models can be applied to future machines to make firm predictions for the effects of different RMP configurations in ITER; this will be the subject of future work. Indeed, based upon the validation of numerical tools with MAST data, assessments of the 3D midplane corrugation and rotation braking have been made for ITER. The midplane displacements are predicted, both with 3D equilibrium modelling and nonlinear resistive MHD codes, to be comparable for $n_{\text{RMP}} = 3$ and 4 fields and within the allowable limits anticipated for plasma facing component heat loading [34]. Quasi-linear MARS-Q simulations of the RMP induced torques show that $n_{\text{RMP}} = 3$ and 4 RMPs produce similar edge braking, but neither are predicted to have a detrimental effect on the core plasma [55]. Finally, it is worth pointing out that vacuum calculations for ITER [16] suggest that the toroidal asymmetry of the lobe structures is far higher for an $n_{\text{RMP}} = 4$ configuration than $n_{\text{RMP}} = 3$ due to an interference of the $n_{\text{RMP}} = 4$ and $n_{\text{RMP}} = 5$ components of the spectrum, potentially resulting in an asymmetric heat loading of the ITER divertor. Furthermore, the wetted area for an $n_{\text{RMP}} = 3$ footprint is predicted to be approximately twice as large as for an $n_{\text{RMP}} = 4$ RMP, favouring the use of $n_{\text{RMP}} = 3$ non-axisymmetric fields in ITER.

Overall, non-axisymmetric fields with toroidal mode number of $n_{\text{RMP}} = 3$ or 4 are optimal for RMP ELM control in MAST since they have less detrimental effects on the power

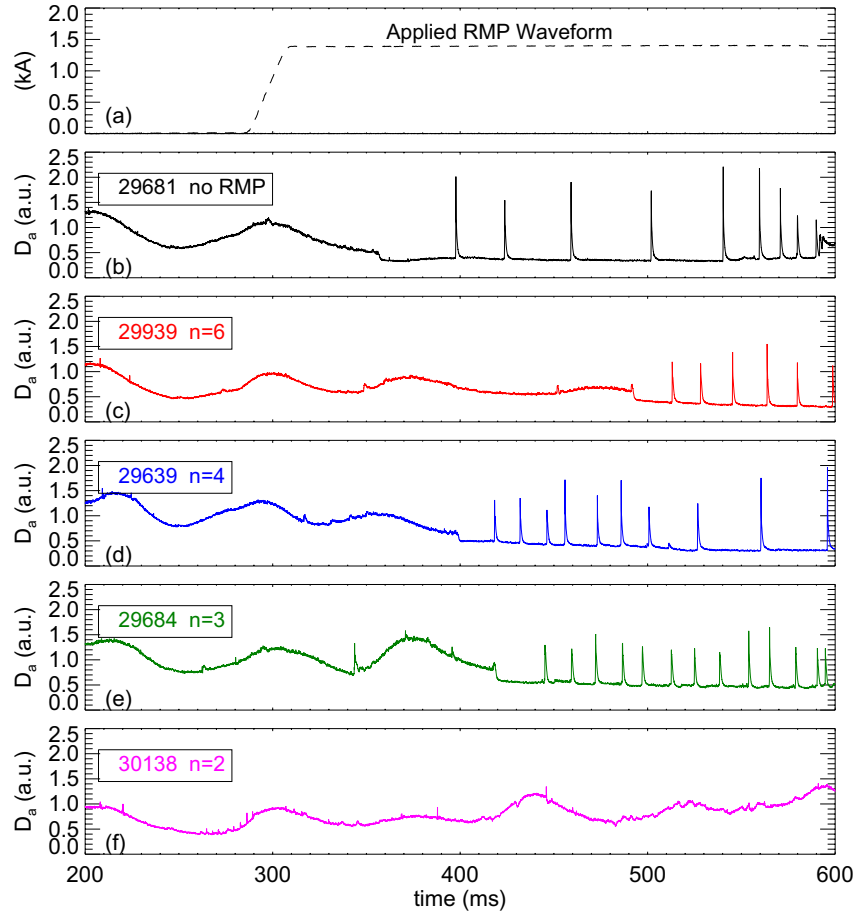


Figure 18. Timetraces of the D_α emission for MAST plasmas with (b) no RMP and (c)–(f) with $n_{\text{RMP}} = 6, 4, 3, 2$ respectively. The RMP waveform is also shown and $P_{\text{NBI}} = 1.5$ MW.

Table 1. Summary of the merits of the various n_{RMP} RMP configurations in MAST for various criteria ordered from the top to bottom, firstly in consideration of safe operation of ITER, and secondly in terms of the most critical for successful operation to $Q = 10$. Note that here the criteria on H-mode access is based upon measurements made with the same coil current rather than fixed b_{res}^r , whereas the criteria for midplane corrugation, lobe structures and rotation braking are taken from cases with the same b_{res}^r . The optimal RMP configuration is highlighted in bold text against each criterion.

Criterion	$n_{\text{RMP}} = 2$	$n_{\text{RMP}} = 3$	$n_{\text{RMP}} = 4$	$n_{\text{RMP}} = 6$
Locked mode threshold	Lowest			Highest
Reduction in q_{peak}	Reduction scales with increase in f_{ELM} in all cases			
Critical b_{res}^r to mitigate ELMs	No data	Lowest		Highest
† I_{coil} for same b_{res}^r (separatrix)	Lowest			Highest
* Power for H-mode	Highest		Lowest	
† Midplane displacement	No data	Least		Most
† Lobe structures	No data	Shortest		Longest
Pedestal structure	Height reduces and width increases in all cases			
† Infinite- n stability	Region and growth rate scales with b_{res}^r in all cases			
† Rotation braking	Strongest			Weakest

* For constant in-vessel coil current † For constant resonant field at the separatrix

to access H-mode, distortions to the magnetic configuration and the plasma rotation, whilst still having a low threshold for an effect on the pedestal and ELMs and a higher tolerance to locked modes than low- n_{RMP} RMPs. The fact that the optimal n_{RMP} can be tuned depending on which ancillary plasma effect is considered most important strongly suggests that ITER should retain the capability to operate with RMPs having a range of different mode numbers and spectra to maximise the likelihood that the in-vessel coils will be able

to control the ELMs to ensure an adequate lifetime of the plasma facing components and simultaneously have minimal deleterious effect on the plasma performance.

Acknowledgments

This project has received funding from the European Unions Horizon 2020 research and innovation programme under grant agreement number 210130335 and from the RCUK Energy

Programme [grant number EP/I501045]. To obtain further information on the data and models underlying this paper please contact PublicationsManager@ccfe.ac.uk. The views and opinions expressed herein do not necessarily reflect those of the European Commission.

References

- [1] Connor J.W. 1998 *Plasma Phys. Control. Fusion* **40** 531
- [2] Snyder P.B. 2002 *Phys. Plasmas* **9** 2037
- [3] Wilson H.R. 2006 *Plasma Phys. Control. Fusion* **48** A71
- [4] Loarte A. *et al* 2003 *Plasma Phys. Control. Fusion* **45** 1594
- [5] Evans T. *et al* 2004 *Phys. Rev. Lett.* **92** 235003
- [6] Evans T. *et al* 2008 *Nucl. Fusion* **48** 024002
- [7] Jeon Y.M. 2012 *Phys. Rev. Lett.* **109** 035004
- [8] Suttrop W. *et al* 2011 *Phys. Rev. Lett.* **106** 225004
- [9] Suttrop W. *et al* 2011 *Plasma Phys. Control. Fusion* **53** 124014
- [10] Kirk A. *et al* 2012 *Phys. Rev. Lett.* **108** 255003
- [11] Kirk A. *et al* 2013 *Nucl. Fusion* **53** 043007
- [12] Kirk A. *et al* 2013 *Plasma Phys. Control. Fusion* **55** 015006
- [13] Liang Y. *et al* 2010 *Nucl. Fusion* **50** 025013
- [14] Liang Y. *et al* 2013 *Nucl. Fusion* **53** 073036
- [15] Lang P.T. *et al* 2013 *Nucl. Fusion* **53** 043004
- [16] Evans T.E. *et al* 2013 *Nucl. Fusion* **53** 093029
- [17] Schaffer M.J. *et al* 2008 *Nucl. Fusion* **48** 024004
- [18] Becoulet M. *et al* 2008 *Nucl. Fusion* **48** 024003
- [19] Fenstermacher M.E. *et al* 2008 *Phys. Plasmas* **15** 056122
- [20] Daly E. *et al* 2013 *Fusion Sci. Technol.* **64** 168
- [21] Wade M.R. *et al* 24th IAEA Fusion Energy Conf. (San Diego, CA) EX/3-1 2012 www-pub.iaea.org/iaea meetings/41985/24th-Fusion-Energy-Conference
- [22] Haskey S.R. *et al* 2014 *Plasma Phys. Control. Fusion* **56** 035005
- [23] Lanctot M. *et al* 2013 *Nucl. Fusion* **53** 083019
- [24] Chapman I.T. *et al* 2012 *Plasma Phys. Control. Fusion* **54** 105013
- [25] Loarte A. *et al* 2014 *Nucl. Fusion* **54** 033007
- [26] Nardon E. 2007 Edge localized modes control by resonant magnetic perturbations *PhD Thesis Ecole Polytechnique* <http://www.imprimerie.polytechnique.fr/Theses/Files/Nardon.pdf>
- [27] Evans T.E. *et al* 2005 *J. Phys.: Conf. Ser.* **7** 174
- [28] Harrison J.R. *et al* 2014 *Nucl. Fusion* **54** 064015
- [29] Shafer M.W. *et al* 2012 *Nucl. Fusion* **52** 122001
- [30] Jakubowski M.W. 2009 *Nucl. Fusion* **49** 095013
- [31] Nardon E. *et al* 2011 *J. Nucl. Mater.* **415** S914
- [32] Cahyna P. *et al* 2011 *J. Nucl. Mater.* **415** S927
- [33] Thornton A.J. *et al* 2013 *J. Nucl. Mater.* **438** S199
- [34] Chapman I.T. *et al* 2014 *Nucl. Fusion* **54** 083006
- [35] Chapman I.T. *et al* 2014 *Plasma Phys. Control. Fusion* **56** 075004
- [36] Scannell R., Kirk A. and Chapman I.T. 2013 *Plasma Phys. Control. Fusion* **55** 035013
- [37] Tourmianski M. *et al* 2003 *Rev. Sci. Instrum.* **74** 2089
- [38] Nardon E. *et al* 2010 *Nucl. Fusion* **50** 034002
- [39] Kirk A. *et al* 2014 Effect of resonant magnetic perturbations on low collisionality discharges in MAST and a comparison with ASDEX Upgrade in preparation
- [40] Huysmans G.T.A. *et al* 2009 *Plasma Phys. Control. Fusion* **51** 124012
- [41] Orain F. *et al* 2013 *Phys. Plasmas* **20** 102510
- [42] Pamela S. *et al* 2013 *Plasma Phys. Control. Fusion* **55** 095001
- [43] Dickinson D. *et al* 2011 *Plasma Phys. Control. Fusion* **53** 115010
- [44] Hirshman S.P., van Rij W.I. and Merkel P. 1986 *Comput. Phys. Commun.* **43** 143
- [45] Sanchez R. *et al* 2000 *J. Comput. Phys.* **161** 576
- [46] Liu Y.Q. and Kirk A. Modelling error field correction experiments in MAST *Plasma Phys. Control. Fusion* submitted
- [47] Liu Y.Q. *et al* 2012 *Plasma Phys. Control. Fusion* **54** 124013
- [48] McClements K. and Thyagaraja A. 2006 *Phys. Plasmas* **13** 042503
- [49] Fitzpatrick R. 1998 *Phys. Plasmas* **5** 3325
- [50] Shaing K.C., Sabbagh S.A. and Chu M.S. 2010 *Nucl. Fusion* **50** 025022
- [51] Chapman I.T. *et al* 2013 *Phys. Plasmas* **20** 056101
- [52] Akers R.J. *et al* 2012 *Proc. 39th EPS Conf. on Plasma Physics* P5.088 <http://epsicpp2012.spp.ee.kth.se>
- [53] Liu Y.Q. *et al* 2000 *Phys. Plasmas* **7** 3681
- [54] Kirk A. *et al* 2013 *Plasma Phys. Control. Fusion* **55** 124003
- [55] Liu Y.Q. *et al* 2014 Modelling of toroidal rotation damping in ITER due to external 3D fields in preparation
- [56] Liu Y.Q. 2010 *Phys. Plasmas* **17** 122502
- [57] Ham C.J. *et al* 2014 Modelling of three dimensional equilibrium and stability of MAST plasmas with magnetic perturbations using VMEC and COBRA *Phys. Plasmas* submitted